Effective Thermal Conductivity of Monolithic and Porous Catalyst Supports by the Moment Technique

Kırali Mürtezaoğlu, Esra Oray, Timur Doğu,* Gülsen Doğu, Nurdan Saraçoğlu, and Canan Cabbar

Department of Chemical Engineering, Gazi University, Ankara, Turkey

The axial and radial effective thermal conductivities of a monolithic ceramic catalyst support and of porous alumina pellets were measured using the moment technique. At 180 °C, radial and axial thermal diffusivities were determined as 9.3×10^{-3} and 11.1×10^{-3} $cm^2 \cdot s^{-1}$, respectively. Having pores being filled with hydrogen, the corresponding thermal conductivity values are 0.43 and 0.52 $W \cdot m^{-1} \cdot K^{-1}$, respectively. Experimental results obtained between 110 and 180 °C indicated a negligibly small dependence of effective thermal conductivities on temperature. A proposed model which included the geometrical parameters of the monolith and the thermal conductivity ratio of the ceramic catalyst support to gas was shown to give excellent agreement with experimental results. Thermal conductivities of alumina pellets having bidisperse pore structures were also measured using this dynamic procedure. Experimental effective thermal conductivity values ranged between 0.043 and 0.120 $W \cdot m^{-1} \cdot K^{-1}$ for pellets having porosities between 0.79 and 0.57, respectively.

Introduction

A significant temperature difference may develop between the interior and the external surfaces of porous catalyst pellets due to heat effects of reactions. One of the earlier studies on the effect of temperature gradients on the effectiveness factor is of Tinkler and Metzner (*1*). The relative importance of temperature and concentration gradients in a porous catalyst pellet was extensively studied in the literature (*2*, *3*), and a general criterion was proposed to test the relative significance of such effects.

The temperature distribution in catalytic monoliths, which were used for controlling automobile emissions, are also significant. These temperature variations and transients have a direct effect on automobile emission levels (*4*, *5*).

There are few published data for the thermal conductivity of porous catalysts. Most of the effective thermal conductivity values reported for porous catalysts are in the range of 10^{-2} to 1 $W \cdot m^{-1} \cdot K^{-1}$ (*6-11*).

In this study, the dynamic technique which was previously introduced by Doğu et al. (*10*, *11*) was used to measure the radial and axial effective thermal conductivities of monolithic catalyst supports as well as the effective thermal conductivities of alumina pellets having different porosities.

Experimental Section

Method and Procedure. In the dynamic technique used in this work a cylindrical solid sample with unknown thermal conductivity (monolithic catalyst support or alumina pellets) was placed in the single pellet conduction cell. Details of the cell and the technique were reported elsewhere (*10*, *11*). A bell-shaped temperature–time curve was generated at the upper surface of the sample by initiating an exothermic reaction in the upper chamber of the cell. For this purpose a cylindrical $Pt-Al_2O_3$ catalyst pellet was placed on top of the sample with unknown thermal conductivity (Figure 1).

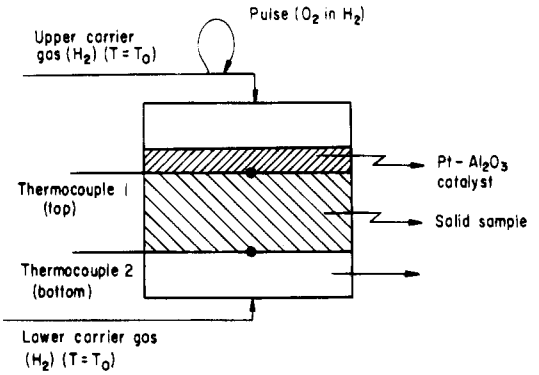

Figure 1. Schematic diagram of the experimental system.

In order to minimize radial temperature variations and to have good contact of the unknown sample with the $Pt-Al_2O_3$ catalyst pellet, these two pellets were pressed into a single cylindrical Teflon mold. The diameter of the cylindrical specimen is 14.5 mm, and the thickness of the wall of the Teflon mold is 1.6 mm. The $Pt-Al_2O_3$ pellet placed in the upper zone of this Teflon mold acts as a heat source. Hydrogen gas streams passed over both end faces of the two-zone cylindrical pellet holder. A pulse of oxygen (6% O_2 in H_2) was injected into the hydrogen stream flowing over the upper face. The oxygen tracer reacted with hydrogen within the upper active zone, and the energy liberated due to reaction in this zone was conducted through the solid sample placed in the lower zone of the unit. The upper surface of the lower chamber (cavity) of the cell is totally exposed to the lower surface of the specimen. In order to eliminate any possible effect of axial conduction through the Teflon mold, the cell was designed in such a way that the Teflon mold was not exposed to either the upper chamber or the lower chamber of the cell (*10*, *11*). Bell-shaped temperature–time curves were measured at the lower end face and at the interface of the solid sample with the $Pt-Al_2O_3$ catalyst pellet (Figure 1). A typical figure showing the variation of the temperature with respect to time at both of the temperature stations is given in Figure 2. In these measurements good contact of the thermocouples with the specimen is important. It was

* To whom correspondence should be addressed at the Department of Chemical Engineering, Middle East Technical University, Ankara, Turkey.

0021-9568/95/1740-0720$09.00/0

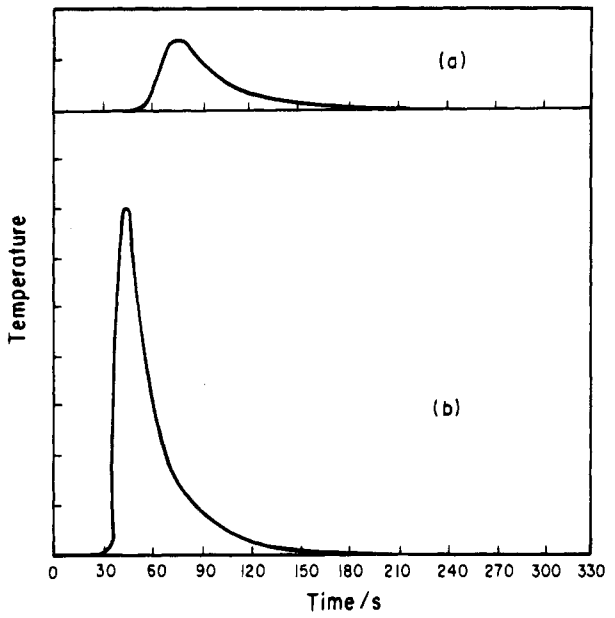

Figure 2. Typical temperature–time curves measured at both end faces of the specimen: (a) bottom face, (b) top face.

shown in the literature (*10*) that the ratio of areas under the curves (zeroth moment ratio) and time delay (first absolute moment difference) of these two bell-shaped curves can be used to evaluate the thermal diffusivity of the sample. For this purpose a single pellet moment technique was used (*10, 11*). This technique was originally proposed for the analysis of diffusion and adsorption in porous solids (*15, 16*). The advantages and limitations of the technique are discussed in refs 15 and 16.

The moments of the bell-shaped temperature–time curves were determined from

$$m_n = \int_0^\infty \left(\frac{T - T_o}{T_o}\right) t^n \, dt \qquad (1)$$

where m_n is defined as the nth moment. In this expression T_o is the oven temperature. The temperature (T) was measured at both end faces of the specimen to evaluate the moments at the bottom and top (m_{0b}, m_{1b}, m_{0t}, m_{1t}).

The following expressions were derived in our previous work (*10, 11*) for the ratio of zeroth moments and the difference of first absolute moments:

$$\left(\frac{m_{0b}}{m_{0t}}\right) = \frac{1}{1 + hL/k_e} \qquad (2)$$

$$\Delta\mu_1 = \left(\frac{m_1}{m_0}\right)_b - \left(\frac{m_1}{m_0}\right)_t = \left(\frac{L^2}{2\alpha_e}\right)\frac{(1 + (1/3)(hL/k_e))}{(1 + hL/k_e)} \qquad (3)$$

where

$$\alpha_e = k_e/\varrho\bar{C} \qquad (4)$$

In this expressions L corresponds to the pellet length, h is the heat transfer coefficient at the bottom face of the pellet, and k_e is the effective thermal conductivity of the specimen. The Biot number (hL/k_e) was then determined from the ratio of zeroth moments using eq 2, and thermal diffusivity α_e was evaluated from the difference of first absolute moments using eq 3. Both of the moment expressions used in the analysis (eqs 2 and 3) are normalized expressions. In eq 2 the zeroth moment at the bottom (m_{0b}) is normalized with respect to the zeroth moment at the top (m_{0t}), and in eq 3 first moments measured at the top and bottom faces of the pellet are normalized with respect to the corresponding zeroth moments. In this technique absolute calibration of the temperature measurements is not necessary for the evaluation of the moments.

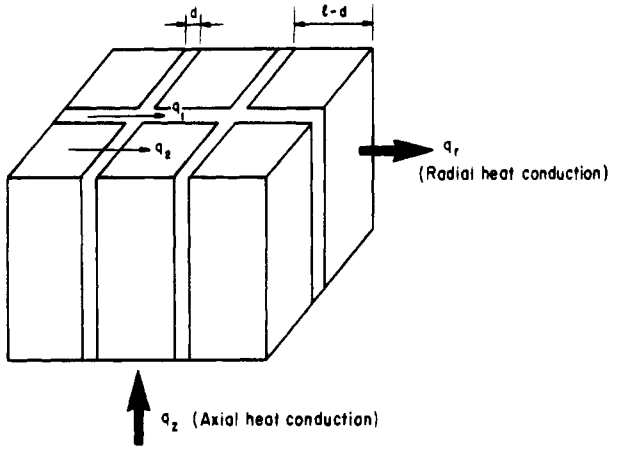

Figure 3. Schematic representation of a monolith.

The conduction cell containing the two-zone pellet holder was placed in a constant temperature oven, and pulse response experiments were conducted at different temperatures. The experimental values of the zeroth and first moments were evaluated by the numerical integration of eq 1, taking $n = 0$ and $n = 1$ using the bell-shaped temperature–time curves obtained at $z = 0$ and $z = L$. Since the tails of these temperature–time curves were not long, possible errors in the evaluation of the moments due to the tailing of these curves were very small. The experiments were repeated at different flow rates of the lower carrier gas stream.

Materials. In the preparation of the platinum–alumina catalyst pellet, Al_2O_3 powder was impregnated by chloroplatinic acid solution. This powder was dried in a vacuum oven at 120 °C, heated to 550 °C for 5 h, and reduced in a hydrogen atmosphere. This powder (0.5% Pt on alumina) was pressed into the cylindrical mold, and a pellet 0.32 cm in length was prepared.

The ceramic monolith used in this work was obtained from Corning. It was cut into desired dimensions, and cylindrical samples were prepared for both radial and axial thermal conductivity measurements. For the measurements of axial effective thermal conductivity, the specimen was placed in the cell in such a way that the channels of the monolith were parallel to the heat flow direction. On the other hand, for the evaluation of the radial effective thermal conductivity, the specimen was prepared in such a way that the channels of the monolith were normal to the axial heat flow direction in the cell. Geometric parameters of the sample (Figure 3) were determined by microscopic examination. Physical properties and the geometric parameters of the monolith used are summarized in Table 1. The open frontal area fraction of the monolith used in this work is 0.75. A similar monolithic support was used in the work of Leclerc and Schweich (*5*). Further information about physical properties of such monoliths is reported in the literature (*4, 12*).

For the experiments conducted with alumina pellets, pellets were prepared by compacting microporous Al_2O_3 powder into the cylindrical mold at different pressures. Physical properties of the alumina pellets used in this study are given in Table 2. As shown in Figure 4 all the pore size distribution curves, determined by a Quantachrome mercury intrusion porosimeter, coincided for pores smaller than 3.5×10^{-3} μm in radius. The volume of these pores

Table 1. Physical Properties and the Dimensions of Monolithic Samples Used

number of cells per cm^2	62
open frontal area (void fraction, ϵ_a)	0.75
apparent density	0.44 $g \cdot cm^{-3}$
wall thickness[a] (d)	0.0178 cm
cell size[a] ($l - d$)	0.1092 cm
$R = (d/l)$	0.14
specific heat of the ceramic material ($\hat{C}$) (5)	1.05 $J \cdot g^{-1} \cdot K^{-1}$
sample length (radial conduction experiments)	0.526 cm
sample length (axial conduction experiments)	0.580 cm

[a] See Figure 3.

Table 2. Physical Properties of the Alumina Pellets Used in This Work

pellet no.	total porosity ϵ	ϵ_i[a]	apparent density (ϱ_g/($g \cdot cm^{-3}$)
1	0.79	0.22	0.56
2	0.76	0.24	0.62
3	0.71	0.31	0.76
4	0.57	0.42	1.10
5	0.55	0.43	1.15

[a] ϵ_i corresponds to pores smaller than 3.5×10^{-3} μm in radius.

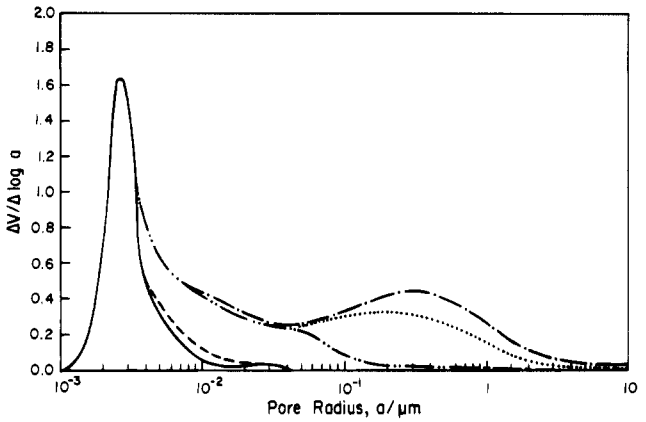

Figure 4. Pore size distributions of the alumina pellets. (—) pellet 5, $\epsilon = 0.55$, (- - -) pellet 4, $\epsilon = 0.57$, (- · -) pellet 3, $\epsilon = 0.71$, (· · ·) pellet 2, $\epsilon = 0.76$, (- · -) pellet 1, $\epsilon = 0.79$.

did not change within the compacting pressure range of this work. We defined these pores as micropores. With this definition of micropores, $\epsilon_i/1 - \epsilon_a$ values were found to be essentially constant for all the pellets. This ratio corresponds to the porosity of microporous grains, and its value is about 0.51 for all the pellets used in this work. As shown in Figure 4, pellets with total porosities of 0.79 and 0.76 have very similar pore size distributions up to a pore radius of 4×10^{-2} μm. Pores larger than this value were easily compressed during pelleting. Pores with radii between 3.5×10^{-3} and 4×10^{-2} μm might be considered as mesopores.

Results and Discussion

Experimental Results for the Radial Thermal Conductivity of the Monolith. The ratio of zeroth moments of the bell-shaped temperature–time curves obtained at the bottom and top of the monolith in the experiments conducted for the measurement of radial effective thermal conductivity are shown in Figure 5. Data reported in this figure showed that at four different temperatures between 110 and 180 °C zeroth moment ratio values were independent of the flow rate and temperature. The mean values, standard deviation of the ratio of zeroth moments, standard error, and 95% confidence values are given in Table 3. The Biot number values were then determined from eq 2 and

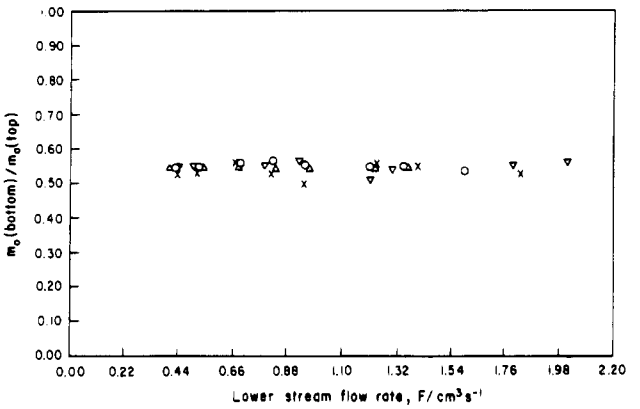

Figure 5. Zeroth moment ratio for radial heat conduction in the monolith ($L = 0.526$ cm): (×) $T = 110$ °C, (○) $T = 140$ °C, (△) $T = 160$ °C, (▽) $T = 180$ °C.

also reported in Table 3. First moment data corresponding to the same set of experiments are given in Figure 6. The mean values, standard deviation, standard error, and 95% confidence values of the first moment difference, $\Delta\mu_1$, are also reported in Table 3. The values of effective thermal diffusivities evaluated from eq 3 at different temperatures showed negligible dependence on temperature (Table 3). Note that the void space of the monolith was filled with hydrogen in these experiments. Neglecting the heat capacity of gas in the pores as compared to the heat capacity of the solid and using the specific heat of the ceramic catalyst support $\hat{C} = 1.05$ $J \cdot g^{-1} \cdot K^{-1}$ (5) and the apparent density value reported in Table 1, the effective radial thermal conductivity was determined, and the values are reported in Table 3.

Modeling of Conduction in the Monolith. Radial heat conduction through a monolith can be expressed as a summation of two parallel heat flux terms, one through the solid phase and the other a series, a heat flux term through the gas and solid phases (Figure 2). Following this idea and using Fourier's law (13) for heat conduction in solid and gas phases, the following relations can be written for the radial heat flux in a monolith:

$$q_r = -k_r \frac{dT}{dr} = q_1 + q_2 \tag{5}$$

$$q_r = -\left[k_s\left(\frac{d}{d + (l - d)}\right) + \left(\frac{1}{R/k_s + (1 - R)/k_g}\right)\left(\frac{(l - d)}{d + (l - d)}\right)\right]\frac{dT}{dr} \tag{6}$$

where

$$R = d/l \tag{7}$$

In this equation k_s and k_g correspond to the thermal conductivities of the gas and solid phases, respectively. The geometric parameters d (wall thickness) and l (cell size) are shown in Figure 3. By the rearrangement of eqs 5–7 the following relation was obtained for the effective radial conductivity in the monolith:

$$\left(\frac{k_r}{k_g}\right) = ZR + \frac{(1 - R)}{R/Z + (1 - R)} \tag{8}$$

where

$$Z = k_s/k_g \tag{9}$$

Table 3. Results Obtained with the Monolith for Heat Conduction in the Radial Direction (Void Space Filled with Hydrogen)

t/°C	110	140	160	180
zeroth moment ratio (mean values) ($m_{0,b}/m_{0,t}$)	0.537	0.551	0.550	0.544
zeroth moment ratio standard deviation	18.7×10^{-3}	8.3×10^{-3}	2.8×10^{-3}	16.5×10^{-3}
zeroth moment ratio standard error	7.1×10^{-3}	2.9×10^{-3}	1.1×10^{-3}	5.8×10^{-3}
zeroth moment ratio 95% confidence	13.9×10^{-3}	5.8×10^{-3}	2.1×10^{-3}	11.4×10^{-3}
Biot number (hL_r/k_r)	0.862	0.815	0.818	0.838
first moment difference $\Delta\mu_1$ (s) (mean values)	10.36	10.21	10.51	10.30
first moment difference standard deviation	0.56	0.51	0.52	0.30
first moment difference standard error	0.19	0.18	0.20	0.11
first moment difference 95% confidence	0.37	0.35	0.39	0.20
radial thermal diffusivity/($cm^2 \cdot s^{-1}$)	9.2×10^{-3}	9.5×10^{-3}	9.2×10^{-3}	9.3×10^{-3}
radial effective thermal conductivity k_r/($W \cdot m^{-1} \cdot K^{-1}$)	0.43	0.44	0.43	0.43

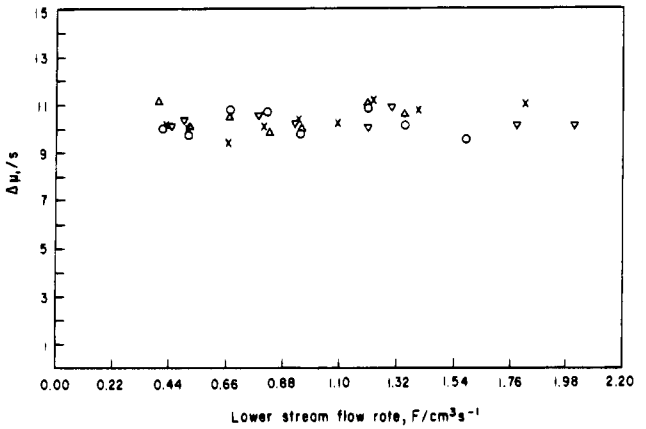

Figure 6. First moment difference for radial heat conduction in the monolith (L = 0.526 cm): (×) T = 110 °C, (○) T = 140 °C, (△) T = 160 °C, (▽) T = 180 °C.

In the case of axial heat conduction, the heat flux may again be expressed as a summation of two parallel heat flux terms, one in the solid phase and the other in the gas phase:

$$q_z = -k_z \frac{dT}{dz} = -\left[k_g \frac{(l-d)^2}{l^2} + k_s \frac{4((l-d)(d/2) + (d/2)^2)}{l^2}\right] \frac{dT}{dz} \quad (10)$$

The following expression was then obtained for the effective thermal conductivity in the axial direction:

$$\left(\frac{k_z}{k_g}\right) = (1-R)^2 + Z(2R - R^2) \quad (11)$$

For the monolith used in this study the value of R is 0.14. Using the experimental values of k_r reported in Table 3, the thermal conductivity of the ceramic material (k_s) was determined from eq 8 and listed in Table 4. In this calculation the thermal conductivity of the gas phase (hydrogen in this work) was estimated from the Eucken expression

$$k_g = (C_p + (5/4)R_g)(\mu/M) \quad (12)$$

where the gas viscosity may be obtained from the Chapman–Enskong relation (*13*):

$$\mu = 2.6693 \times 10^{-5}((MT)^{1/2}/\sigma^2\Omega_\mu) \quad (13)$$

Experimental Results for Axial Thermal Conductivity of the Monolith. The ratios of zeroth moments obtained in axial conduction experiments conducted with the monolith are shown in Figure 7. Using the data reported in this figure, the Biot numbers were determined.

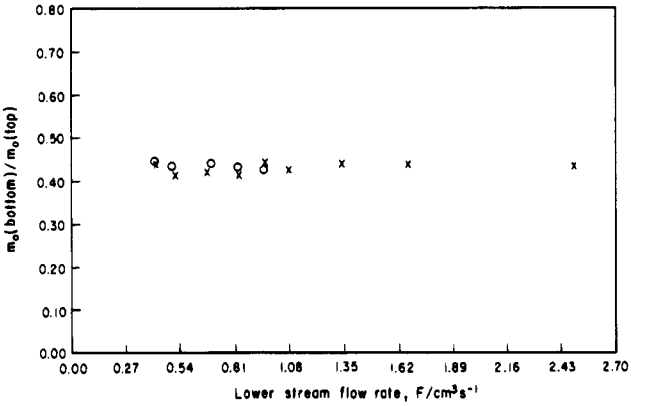

Figure 7. Zeroth moment ratio for axial heat conduction in the monolith (L = 0.58 cm): (×) T = 160 °C, (○) T = 180 °C.

Table 4. Thermal Conductivity of the Ceramic material, k_s, from Radial Heat Conduction Experiments with the Monolith (Void Space Filled with Hydrogen)

t/°C	110	140	160	180
radial effective thermal conductivity k_r/($W \cdot m^{-1} \cdot K^{-1}$)	0.43	0.44	0.43	0.43
gas phase (hydrogen) thermal conductivity/($W \cdot m^{-1} \cdot K^{-1}$)	0.209	0.220	0.226	0.232
thermal conductivity of the solid (ceramic) phase of the monolith/($W \cdot m^{-1} \cdot K^{-1}$) (using eq 8)	1.61	1.57	1.46	1.42
$Z = k_s/k_g$	7.70	7.14	6.46	6.12

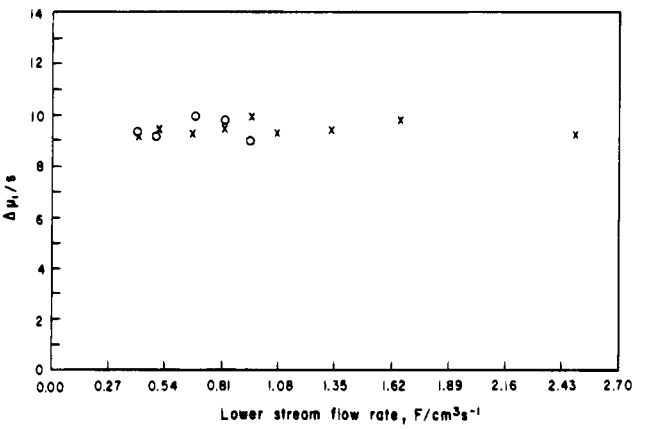

Figure 8. First moment difference for axial heat conduction in the monolith (L = 0.58 cm): (×) T = 160 °C, (○) T = 180 °C.

First moment results for the corresponding experiments conducted at 160 and 180 °C are given in Figure 8. Using these data and following the procedure outlined for the radial thermal conductivity experiments, axial effective thermal conductivity values of the monolith were experimentally determined. Axial thermal conductivities were also predicted from the model expression (eq 11). Experimental and predicted values are both given in Table 5. The

Table 5. Experimental and Predicted (Eq 7) Axial Effective Thermal Conductivity Values of the Monolith (Hydrogen Gas Fills the Void Space)

t/°C	160	180
zeroth moment ratio (mean values)	0.429	0.435
zeroth moment ratio standard deviation	11.4×10^{-3}	5.9×10^{-3}
zeroth moment ratio standard error	3.8×10^{-3}	2.7×10^{-3}
zeroth moment ratio 95% confidence	7.4×10^{-3}	5.2×10^{-3}
first moment difference $\Delta\mu_1$ (s) (mean values)	9.45	9.42
first moment difference standard deviation	0.26	0.41
first moment difference standard error	0.09	0.18
First moment difference 95% confidence	0.17	0.35
experimental values of axial thermal diffusivity/($cm^2 \cdot s^{-1}$)	11.0×10^{-3}	11.1×10^{-3}
experimental values of axial thermal conductivity k_z/($W \cdot m^{-1} \cdot K^{-1}$)	0.51	0.52
model prediction of k_z/($W \cdot m^{-1} \cdot K^{-1}$) (eq 11)	0.55	0.54

Table 6. Radial and Axial Thermal Conductivities of the Monolith at 180 °C (Nitrogen Being the Gas Filling the Void Space) (Calculated and Published Values)

gas thermal conductivity k_g (nitrogen)	0.034 $W \cdot m^{-1} \cdot K^{-1}$
solid thermal conductivity k_s	1.42 $W \cdot m^{-1} \cdot K^{-1}$
radial effective thermal conductivity k_r (predicted by eq 8)	0.23 $W \cdot m^{-1} \cdot K^{-1}$
radial thermal conductivity reported in the literature (*5*)	0.25 $W \cdot m^{-1} \cdot K^{-1}$
axial effective thermal conductivity k_z (predicted by eq 11)	0.39 $W \cdot m^{-1} \cdot K^{-1}$
axial effective thermal conductivity reported in the literature (*5*)	0.38 $W \cdot m^{-1} \cdot K^{-1}$

mean values, standard deviation, standard error, and 95% confidence values of both zeroth moment ratios and first moment differences corresponding to axial conduction experiments are also given in this table.

Some typical values of k_z and k_r are reported by Leclerc and Schweich (*5*). In order to make a comparison of these values with the model predictions of this work, axial and radial effective thermal conductivity values were calculated, with nitrogen filling the void space of the monolith, using eqs 11 and 8, respectively. In this calculation the k_s value reported in Table 4 was used. These predicted thermal conductivities and the thermal conductivities reported by Leclerc and Schweich are given in Table 6. Results shown in Tables 5 and 6 indicate that eqs 8 and 11 can be successfully used in the prediction of radial and axial effective thermal conductivities of the monolith.

Effective Thermal Conductivity of Alumina Pellets. Effective thermal conductivities of alumina pellets of different porosities were measured using the same procedure. Experiments were conducted in a hydrogen atmosphere at 110 °C. The ratio of zeroth moments and difference of first absolute moments are given in Figures 9 and 10, respectively. Effective thermal diffusivities evaluated from these data by use of eqs 2 and 3 are reported in Table 7. Variation of thermal diffusivity with porosity is due to an increase of both thermal conductivity and density with a decrease in porosity. These two effects first cause a slight decrease in thermal diffusivity with a decrease in porosity. On the other hand, for very dense pellets an increase of effective thermal conductivity with a decrease in porosity becomes more significant and thermal diffusivity also increases. Using the density values reported in Table 2 and the specific heat of alumina $\hat{C}$ = 0.90 $J \cdot g^{-1} \cdot K^{-1}$, thermal conducitivities of the pellets were determined from eq 4, and the values are reported in Table 7. These values are in good agreement with the previously published effective thermal conductivities of porous catalysts (*10*, *14*). Effective thermal conductivity values of porous alumina pellets were found to be smaller than the effective thermal conductivity of the monolith. The contact resistance between the grains of pressed alumina pellets is expected to have a significant contribution to the overall conduction resistance in porous pellets.

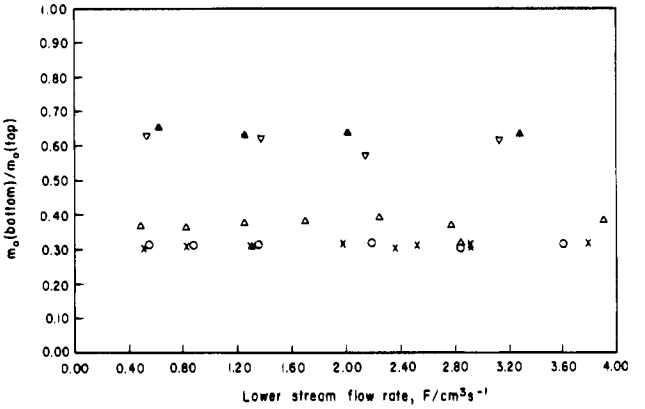

Figure 9. Zeroth moment ratio for conduction in alumina pellets (L = 0.24 cm, T = 110 °C): (×) pellet 1, (○) pellet 2, (△) pellet 3, (▽) pellet 4, (▲) pellet 5.

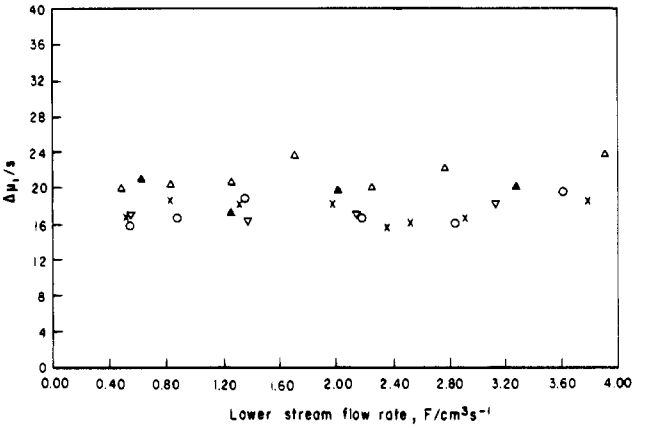

Figure 10. First moment difference for conduction in alumina pellets (L = 0.24, T = 110 °C): (×) pellet 1, (○) pellet 2, (△) pellet 3, (▽) pellet 4, (▲) pellet 5.

Table 7. Thermal Conductivities of Alumina Pellets (T = 110 °C, Void Volume Filled by Hydrogen, L = 0.24 cm)

pellet no.	ϵ	$10^4\alpha_e$/($cm^2 \cdot s^{-1}$)	k_e/($W \cdot m^{-1} \cdot K^{-1}$)
1	0.79	8.79	0.044
2	0.76	8.45	0.047
3	0.71	7.53	0.052
4	0.57	12.43	0.120
5	0.55	11.18	0.116

Results of this work showed that the moment technique used here is a very effective procedure for the precise evaluation of effective diffusivity and the thermal conductivity of porous catalysts and monoliths. The technique might as well be used for any solid sample. It was also shown that the model expressions derived for radial and axial thermal conductivities of a monolith may be successfully used in the prediction of these values.

Acknowledgment

The authors would like to thank Mr. Göksel Özkan for his contributions to this work and Corning who supplied the monolith.

Notation

a	pore radius
C_p	molar heat capacity of the fluid
$\hat{C}$	specific heat
d	wall thickness of the monolith (see Figure 3)
h	heat transfer coefficient
k_e	effective thermal conductivity
k_r	effective radial thermal conductivity of the monolith
k_g	thermal conductivity of the gas
k_s	thermal conductivity of the solid
k_z	effective axial thermal conductivity of the monolith
l	cell dimension (Figure 3)
L	pellet length
m_n	nth moment defined by eq 1
$m_{0,b}$	zeroth moment at the bottom of the sample
$m_{0,t}$	zeroth moment at the top of the sample
M	molecular weight
q_r	radial heat flux
q_z	axial heat flux
R	d/l
R_g	universal gas constant
t	time
T	temperature
T_o	oven temperature
z	axial direction
Z	k_s/k_g

Greek Letters

ϵ	porosity
ϵ_i	microporosity
α_e	effective thermal diffusivity
μ_1	first absolute moment
μ	gas viscosity
$\Delta\mu_1$	difference of first absolute moments
σ	Lennard-Jones parameter

Literature Cited

(1) Tinkler, J. D.; Metzner, A. B. *Ind. Eng. Chem.* **1961**, *53*, 663–668.
(2) Doğu, T. *Can. J. Chem. Eng.* **1985**, *63*, 37–42.
(3) Doğu, T.; Doğu, G. *AIChE J.* **1984**, *30*, 1002–1004.
(4) Oh, S. H.; Cavendish, J. C. **1982**, *21*, 29–37.
(5) Leclerc, J. P.; Schweich, D. In *Chemical Reactor Technology for Environmentally Safe Reactors and Products*; deLasa, H. I., Doğu, G., Ravella, A., Eds.; NATO ASI Series E; Kluwer Academic Publishers: Dordrecht, The Netherlands, 1992; Vol. 225, pp 547–567.
(6) Sehr, R. A. *Chem. Eng. Sci.* **1958**, *9*, 145–152.
(7) Krupiczka, R. *Int. Chem. Eng.* **1967**, *7*, 122–145.
(8) Jiratova, K.; Horak, J. *Int. Chem. Eng.* **1978**, *18*, 297–304.
(9) Masamune, S.; Smith, J. M. *J. Chem. Eng. Data* **1963**, *8*, 54–58.
(10) Doğu, G.; Mürtezaoğlu, K.; Doğu, T. *AIChE J.* **1989**, *35*, 683–685.
(11) Doğu, G.; Cabbar, C.; Doğu, T. *Chem. Eng. Commun.* **1991**, *102*, 149–159.
(12) Lachman, I. M.; McNally, R. N. *Chem. Eng. Prog.* **1985**, Jan, 29–31.
(13) Bird, R. B.; Stewart, W. E.; Lightfoot, E. N. *Transport Phenomena*; John Wiley and Sons Inc.: New York, 1960.
(14) Mischke, R. A.; Smith, J. M. *Ind. Eng. Chem. Fundam.* **1982**, *1*, 288–291.
(15) Doğu, G.; Smith, J. M. *AIChE J.* **1975**, *21*, 58–61.
(16) Doğu, G.; Smith, J. M. *Chem. Eng. Sci.* **1976**, *31*, 123–134.

Received for review August 8, 1994. Accepted March 21, 1995.[⊗]

JE9401631

[⊗] Abstract published in *Advance ACS Abstracts*, June 1, 1995.